Structural characteristics of Bi 2 O 2 CO 3 nanosheets synthesized by nano-pulsed discharges in water

A V Nomine, J. Ghanbaja, A. Redjaimia, T. Belmonte

Structural characteristics of $Bi_2O_2CO_3$ nanosheets synthesized by nano-pulsed discharges in water

AV Nomine, J Ghanbaja, A. Redjaimia, and T.Belmonte*

Université de Lorraine, CNRS, IJL, F-54000 Nancy, France

* Corresponding author.

E-mail address: thierry.belmonte@univ-lorraine.fr

Keywords

Discharges in liquids ; Nanoparticles ; non-equilibrium ; immiscible elements ; nanoalloys

Synopsis

Bismuthene OxyCarbonate nanosheets, synthesized by nanosecond pulsed discharges in water, adopt a pinacoid shape dictated by the 4/m2/m2/m point group. The growth mechanism based on the presence of jogs, both on the terraces and fronts, was clarified.

Abstract

A comprehensive analysis of $Bi_2O_2CO_3$ nanosheets, which were synthesized using nanosecond-pulsed discharges in water between bismuth electrodes, was conducted in order to investigate the crystallographic features of this material. Analyses, employing electron diffraction, XRD and EELS techniques, revealed the presence of a stoichiometric tetragonal $Bi_2O_2CO_3$ structure, labelled BOC in this study. This structure crystallizes in the body-centred tetragonal Bravais lattice and belongs to the I4/mmm space group (139), with the following lattice parameters: a = 3.91 Å and c = 13.77 Å.

The nanosheets adopt squared shapes. This shape is dictated by the symmetry elements of its point group (4/mmm) under the prevailing local conditions. From the energetic point of view, this shape, dictated by the 4/m2/m2/m point group, therefore a pinacoid, corresponds to an absolute extremum, an indicator of the stability of this BOC nanosheets.

Most nanosheets are crossed by equal inclination fringes or bend contours. These bend contours reflect the fact that the BOC nanosheets are so thin and/or contain crystal defects that they bent elastically leading to rotation of the lattice planes towards diffracting Bragg position.

In this study, the diffraction patterns corresponding to bend-contours intersecting along the [001] zone axis attracts attention. Satellite diffraction lattices are superimposed on the diffraction pattern of the BOC crystallographic structure. The origin of these lattices is essentially attributed to two phenomena: multiple diffraction and local disorder-order transformations of the BOC crystal structure, passing from a body centered tetragonal to a primitive Bravais lattice.

A mechanism related to the ledge mechanism (kinks and jogs), explaining the formation of nanosheets in metallic matrix, has been adapted and proposed for the formation of the BOC nanosheets in water. When the nanosheets are removed from water, they get carbonated once in the air, leading to formation of BOC, inheriting the nanosheet morphology.

1. Introduction

Nanoscale materials have garnered substantial interest owing to their distinctive properties and potential applications across various domains. Among these, bismuth oxycarbonate (BOC) $Bi_2O_2CO_3$, also known as bismutite or bismuth subcarbonate, and sometimes represented as $(BiO)_2CO_3$, has emerged as an exceptional material. BOC exhibits diverse morphologies, including sponge-like hierarchical microspheres, nanoflowers, nanosponges, and nanoplates, as reported in various studies (Zheng *et al*. 2010; Madhusudan *et al*. 2013; Zhao *et al*. 2011; Tian *et al*. 2022; Ni *et al*. 2016). These morphologies are efficiently used as a visible-light-driven photocatalyst for the degradation of organic dyes such as rhodamine B, methylene blue, and methyl orange. This material also has captured significant interest due to its remarkable electronic, optical, and sensing properties (Wang *et al*. 2017; Huang *et al*. 2014; Umar *et al*. 2016).

Numerous methods have been documented in the literature for synthesizing this subcarbonate material. These methods encompass hydrothermal processes (Zheng *et al*. 2010), solution precipitation techniques (Chen *et al*. 2012), and a template-free approach involving Ostwald ripening (Dong *et al*. 2011). These methods primarily yield three-dimensional morphologies or thick plates. Nevertheless, achieving extremely thin, free-standing nanosheets with a thickness below 10 nm has proven to be a formidable challenge. A recent groundbreaking study by Gupta *et al*. (2022) introduced an innovative strategy to overcome this challenge. They successfully produced laterally large, atomically-thin 2D $Bi_2O_2CO_3$ nanosheets using a sonochemically-assisted template-free synthesis method through liquid-phase exfoliation (LPE) treatment of bulk Bi powder.

In addition, Qin *et al*. (2021) reported on $Bi_2O_2CO_3$ nanosheets with a remarkable thickness of 4-5 nm. These nanosheets were obtained spontaneously through the transformation of two-dimensional bismuthene nanosheets via electrochemical exfoliation. Remarkably, after exposing the bismuthene nanosheets to ambient air for a few days, they underwent a transformation into thin $Bi_2O_2CO_3$ nanosheets.

In this context, our study introduces an innovative approach that enables the creation of free-standing $Bi_2O_2CO_3$ nanosheets with an average thickness below 10 nm. This method employs nanosecond-pulsed discharges occurring between two bismuth electrodes submerged in water, resulting in nanosheet formation through electrode erosion. Initially, metallic nanosheets are generated via the erosion of the Bi electrodes. The metallic state of these initial nanosheets was demonstrated thanks to optical emission spectroscopy measurements and further comparison with submerged discharges in liquid nitrogen (Nominé *et al*. 2021). Subsequently, these nanosheets undergo oxidation in the water, transforming into Bi_2O_3. Upon exposure to air, these nanosheets undergo carbonation, leading to their conversion into tetragonal $Bi_2O_2CO_3$.

A mechanism akin to the ledge mechanism, which elucidates the generation of thin plates within a metallic matrix, has been adapted and proposed to account for the formation of tetragonal $Bi_2O_2CO_3$ nanosheets in other studies (Kabbara *et al*. 2019; Porter *et al*. 2009; Morin *et al*. 2011). When water is removed, the nanosheets experience carbonation, resulting in the formation of tetragonal $Bi_2O_2CO_3$, while retaining their nanosheet morphology. As far as our knowledge extends, this marks the inaugural endeavor in synthesizing such layered $Bi_2O_2CO_3$ nanosheets through nanosecond-pulsed electrical discharges in liquids, followed by carbonation in the atmosphere.

The produced nanosheets typically display widths ranging approximately from 1 to 10 μm and thicknesses ranging from 3 to 20 nm. Since this represents the first instance of $Bi_2O_2CO_3$ synthesis through this particular technique, a comprehensive investigation was undertaken to characterize these

nanosheets in great detail. Various techniques, including, X-ray Diffraction (XRD), Electron diffraction (SAED, CBED and Microdiffraction modes), Transmission electron Microscopy imaging (HRTEM-High-Resolution Transmission Electron Microscopy, STEM-Scanning Transmission Electron Microscopy, HAADF-High Angle Annular Dark Field), Spectroscopies (EELS-Electron Energy-Loss Spectroscopy, EDS-Energy Dispersive Spectroscopy microanalysis), FIB (Focused Ion Beam), and AFM (Atomic Force Microscopy), were employed to elucidate the crystal structure in which these squared nanosheets crystallize.

It turns out that important features, actually observed by TEM in some previous reports about $Bi_2O_2CO_3$ (Gupta *et al*. 2022; Li *et al*. 2022), and other Bi-containing nanosheets (Xu *et al*. 2013; Zhou *et al*. 2010), were not discussed. For instance, additional spots on electron diffraction patterns were reported but the origin of these interesting features remains unclear. The purpose of this work is to provide a complete description of the structural characteristics of $Bi_2O_2CO_3$ nanosheets. Simulated of the crystal structure of the BOC has been conducted under different software, more particularly, by Vesta and CrystalMaker, *etc*.

2. Experimental setup

Bismuthene oxycarbonate nanosheets were synthesized through the electrical discharges in dielectric liquids (EDDL) process. Initially, bulk bismuth rod electrodes underwent chemical etching, followed by erosion through nanosecond-pulsed discharges in MilliQ water. The procedure began by shaping the Bi rod into a conical structure featuring a 10 mm base diameter. Then, the electrodes were meticulously polished using 1200-grit paper and subsequently rinsed with tap water. Following this, the electrodes were immersed in a 5% Nital chemical etching solution for a duration of 20 minutes.

After the etching phase, the Bi electrodes underwent rinsing, were securely positioned in electrode holders, and were immersed in a 30 ml glass beaker filled with ultra-pure water (conductivity: 0.055 µS cm^{-1}) chosen as the dielectric liquid. The distance between the electrodes was consistently maintained by precise adjustments using micrometric screws. A high positive voltage was supplied by a DC power source (Technix SR15-R-1200) to a solid-state switch (HTS-301-03-GSM), which was under the control of a function generator, generating high voltage pulses.

In this setup, the power electrode received the electrical signal, while the second electrode acted as the cathode and remained grounded during the process. Pulses with a voltage of +5 kV, frequency of 10 Hz, and pulse width of 75 ns were applied to the power electrode over a duration of 90 minutes. This process aimed to achieve a concentration of 15 mg within a water volume of 30 ml.

For characterizing the products resulting from the electrode erosion, carbon and holey carbon grids were utilized as substrates for electron microscopy analysis. The nanosheets were collected by immersing a TEM grid in a solution containing the synthesized $Bi_2O_2CO_3$ nanosheets.

3. Results

3.1 Morphology of the BOC

Throughout the synthesis process, the electrodes undergo erosion. Through the comparison of electrode weights before and after a series of discharges, we calculated an average erosion rate of approximately 0.2 µg per discharge. **Fig. S1**, as indicated in our supplementary information, presents low magnification SEM images showcasing the as-synthesized BOC nanosheets at different magnifications (**Figs. S1a-c**). These figures are accompanied by lateral size distribution data (**Fig. S1d**). Typically, our synthesis process yields nanosheets with dimensions around 4-5 µm, as consistently observed in numerous

experiments. However, it is worth noting that on occasion, larger nanosheets, approximately 20 µm in size, have also been observed (**Fig. S2**).

Fig. 1 showcases TEM and STEM images of the synthesized nanosheets after 30 min of treatment. The most commonly encountered nanosheet morphologies are squared nanosheets with sizes ranging from 1 to 10 µm (**Figs 1a-c**). To elucidate the lamellar arrangement of the nanosheets, cross-sectional view of the BOC nanosheet was attained through the application of the Focused Ion Beam (FIB) technique along [100] zone axes utilizing the HAADF STEM mode, which provides a Z-contrast image (**Fig. 1d**).

Importantly, these structures exhibit remarkable stability under ambient air conditions, and observations conducted over a span of more than a year consistently yielded identical outcomes.

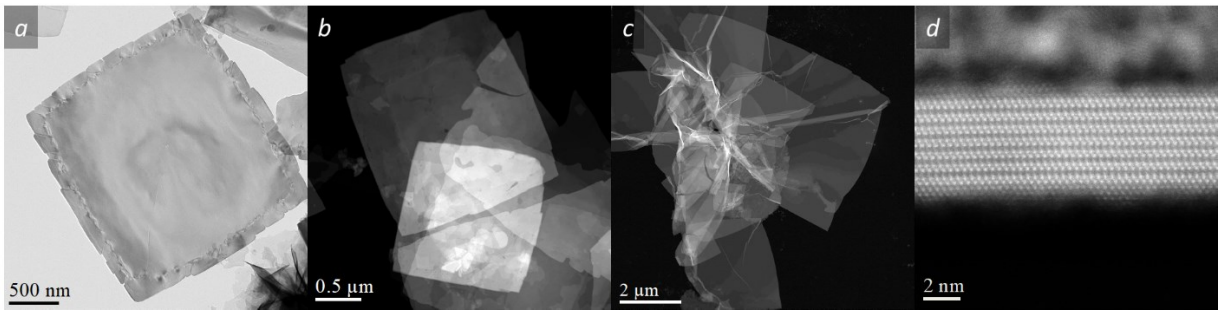

Figure 1
a) BF TEM and b-c) HAADF STEM micrographs showing $Bi_2O_2CO_3$ with most commonly encountered nanosheet morphologies, d) high resolution STEM FIB cross section micrograph of a BOC nanosheet along [100] zone axes.

AFM (**Fig. S3**) and EELS (**Figs. S4, S5**) analyses were conducted to ascertain the thicknesses of the produced nanosheets. The thickness estimation of a single layer was carried out by considering the t/λ ratio obtained from EFTEM (Energy Filtered Transmission Electron Microscopy), which ranged from 0.03 (**Figs. S4a,b**) to 0.24 (**Fig. S5**). The value of λ, representing the mean free path in nanometers, was theoretically calculated using the formula (Carter *et al*. 2009; Oh-Ishi *et al*. 2020):

$$\lambda = \frac{106 \times F\left(\frac{E_0}{E_m}\right)}{\ln\left(2\beta\frac{E_0}{E_m}\right)}$$

where λ is the mean free path, E_0 is the energy in kilo-electron volts (keV), β is the collection angle in milliradians (mrad), F is the relativistic correction factor, and E_m is the average energy loss in electron volts (eV). For a material with an average atomic number Z, E_m is given by:

$$E_m = 7.6 \times Z^{0.36}$$

Considering the specific material $Bi_2O_2CO_3$ with an average atomic number Z of 32.25, the calculated mean free path is 86.5 nm. With this calculated value, the estimated thickness of a thinnest nanosheets falls within the range of 3-5 nm (**Figs. S4a-b**). For the thickest nanosheets present on a substrate after synthesis (as shown in **Fig. S5**), this estimation extends up to 20 nm. Significantly, this estimation aligns exceptionally well with the AFM measurements presented either in subsequent sections (see **Fig. S3**) or in the earlier discussion, substantiating the reliability of our thickness estimation technique.

3.2 Crystal structure identification

In TEM, the microdiffraction pattern corresponds to the intersection of the Ewald sphere with the zeroth and first reciprocal lattice layers recorded along the $\langle uvw \rangle$ direction, a zone axis of the phase that we are attempting to identify. To these zeroth and first layers correspond the zero-order Laue zone (ZOLZ) and to the first-order (FOLZ) order Laue zone, respectively. The analysis of microdiffraction is based on the net and ideal symmetries of the ZOLZ and of the entire pattern, which is represented as WP = (ZOLZ + FOLZ). The net symmetry primarily pertains to the position of the reflections in the pattern, while the ideal symmetry encompasses not only the positions but also the intensities of these reflections. These symmetries, observed along specific zone axes, are connected to the crystal systems and to the point groups.

Fig. 2a shows an experimental microdiffraction pattern recorded along the $\langle uvw \rangle$ zone axis of the BOC particle. Taking into account both the position and the intensity of the reflections of this zone-axis pattern (ZAP), it is clear that the highest ideal symmetry for this phase is $\{$**(4mm), 4mm**$\}$. This symmetry is recorded along $\langle uvw \rangle = \langle 001 \rangle$ or $\langle uvw \rangle = [001]$ for the cubic or the tetragonal systems, respectively.

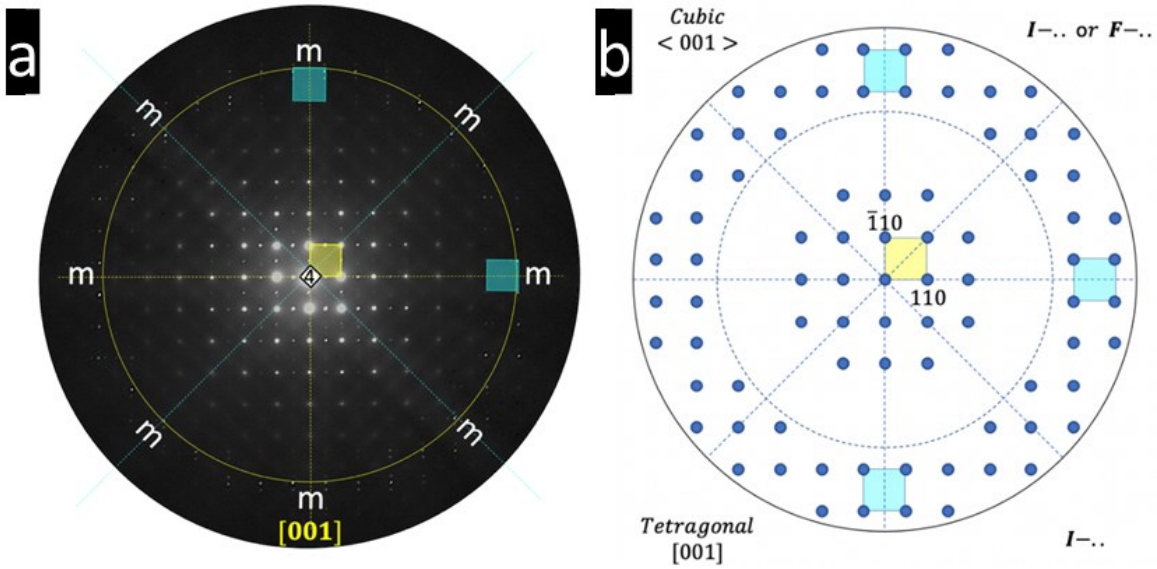

Figure 2
a) Experimental electron microdiffraction patterns recorded along the <001> or [001 zone axis, showing the $\{\underline{4}mm), \underline{4}mm\}$ ideal symmetry for the whole pattern WP = (ZOLZ + FOLZ). One can notice the half shift between the reflection nets of the ZOLZ and the FOLZ along the horizontal and orthogonal mirrors. **b)** Simulated microdiffraction patterns along <001> or [001], highlighting the partial diffraction symbol, common to both crystal systems, cubic and tetragonal, respectively

By taking into account the relative positions of the reflections belonging to the ZOLZ and to the FOLZ, it comes out that the partial diffraction symbol is $I-..$ for the tetragonal system and $I-..$ or $F-..$ for the cubic system (**Fig. 2b**). The extra reflections forming a square net in the ZOLZ are not taken into account for the determination of the partial diffraction symbol. The origin of these satellite reflections will be treated in detail in paragraph 3.6.

The simulated diffraction pattern (**Fig. 2b**) highlights the partial diffraction symbol, common to both cubic and tetragonal systems. The identified partial diffraction symbol asserts that there is no glide plane along $\langle 001 \rangle$ or $[001]$ if the BOC crystallizes in cubic or tetragonal system, respectively.

The diffraction symbol will be completely identified if the partial diffraction symbols are identified along the $[100]$ and $[110]$ zone axes for the tetragonal system and along the $\langle 110 \rangle$ axis for the cubic

system. Unfortunately, it is quite difficult to record microdiffraction patterns along the latter axes due to the fact that the nanosheet are always flat and almost never edge-on.

To identify the crystal system (cubic or tetragonal), we measured the R_{FOLZ} (the radius of the FOLZ) of the diffraction pattern recorded along ⟨001⟩ (**Figs. 3 and 4a**) and consequently the layer parameter $P_{\langle uvw \rangle}$ which is none other than the parameter a for the cubic system or c for the tetragonal system. The layer parameter $P_{<uvw>}$ is related to R_{FOLZ} by the following equation (Thomas *et al*. 1979):

$$P_{<uvw>} = 2\frac{(L\lambda)^2}{(\lambda)R_{FOLZ}^2}$$

where:

- $P_{<uvw>}$ is the row parameter,
- $\lambda = 2.51\ 10^{-3}$ nm is the wavelength of electrons under accelerating tension, $V = 200$ kV,
- $L = 92.79$ cm is the chamber length of the microscope, working at 200 kV and
- $R_{FOLZ} = 5.6$ mm is the measured radius of the FOLZ (**Figs. 3 and 4a**)

The deduced lattice parameter a from the ZOLZ of the diffraction pattern recorded along ⟨001⟩ or [001] is $a = 0.391$ nm for both the two crystal systems, cubic or tetragonal.

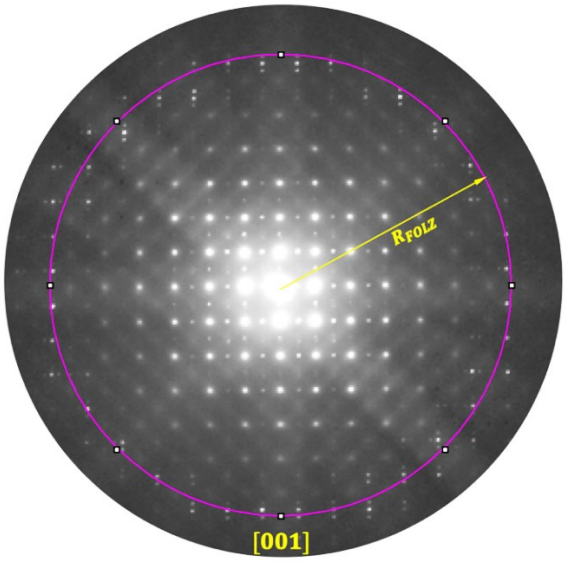

Figure 3
Experimental diffraction pattern recorded along $< 001 >$ for the cubic system or [001] for the tetragonal system pointing out the R_{FOLZ}, the radius of the FOLZ. The latter is related to the range parameter $P_{<001>}$ ($P_{<001>}$ for the cubic system or $P_{[001]}$ for the tetragonal system)

Following the procedure previously mentioned, the calculated row parameter is $P_{<001>} = 1.378$ nm, which is completely different from $a = 0.391$ nm and which, in addition, is not its multiple. If the lattice parameter c is a multiple of a ($c = ka$), this would indicate that we have a reflection extinction induced by the presence of a helicoidal axis parallel to c ($c // < 001 >$).

Through this characterization, we can conclude that the BOC crystallizes in the tetragonal system with a body-centred Bravais lattice. The cubic system is thus eliminated.

Based on the **{(4mm), 4mm}** ideal symmetry of the diffraction pattern recorded along [001], the BOC belongs either to the 4mm or to the 4/mmm point groups, and it would belong to one of the four following space groups, ranked in **Table 1**.

One can notice that the space groups belonging to the body centred tetragonal and having helicoidal axes along [001] are removed. We are left only with two space groups per point group.

Based on the Buxton et *al.* method (Buxton *et al*. 1976), we can achieve the same result by considering the symmetry characteristics of the diffraction pattern obtained in CBED mode (convergent beam electron diffraction) along the zone axis [001]. The symmetries, we are concerned with, are those of the Bright field and of the whole pattern.

Table 1

Possible space groups, candidates for BOC characterization

Point groups	Space groups
$4mm$	$I4mm$ (107) I4cm (109)
$4/mmm$	$I\frac{4}{m}mm$ or $\left(I\frac{4}{m}\frac{2}{m}\frac{2}{m}\right)$ $\left(I\frac{4}{m}\frac{2}{m}\frac{2}{m}\right)$ (139) $I\frac{4}{m}cm$ or $\left(I\frac{4}{m}\frac{2}{c}\frac{2}{m}\right)$ (140)

The symmetry of the whole pattern is 4mm (**Fig. 4a**). To this symmetry, correspond the diffraction group groups $4mm$ and $4mm1_R$. The diffraction group $4mm1_R$ is connected to the holo-symmetric point group $4/mmm$ ($\frac{4}{m}\frac{2}{m}\frac{2}{m}$) or m$\bar{3}$m ($\frac{4}{m}\bar{3}\frac{2}{m}$) while the diffraction point group $4mm$ is connected to the point group $4mm$. The point groups $4/mmm$ and $4mm$ belong to the tetragonal system while the $m\bar{3}m$ belongs to the cubic system. The ZOLZ pattern ideal symmetry is also $4mm$ (**Fig. 4b**).

One of the special features of this method is the precision of the R_{FOLZ} measure (**Fig. 4a**) and therefore of the row parameter and in our case of the lattice parameter c.

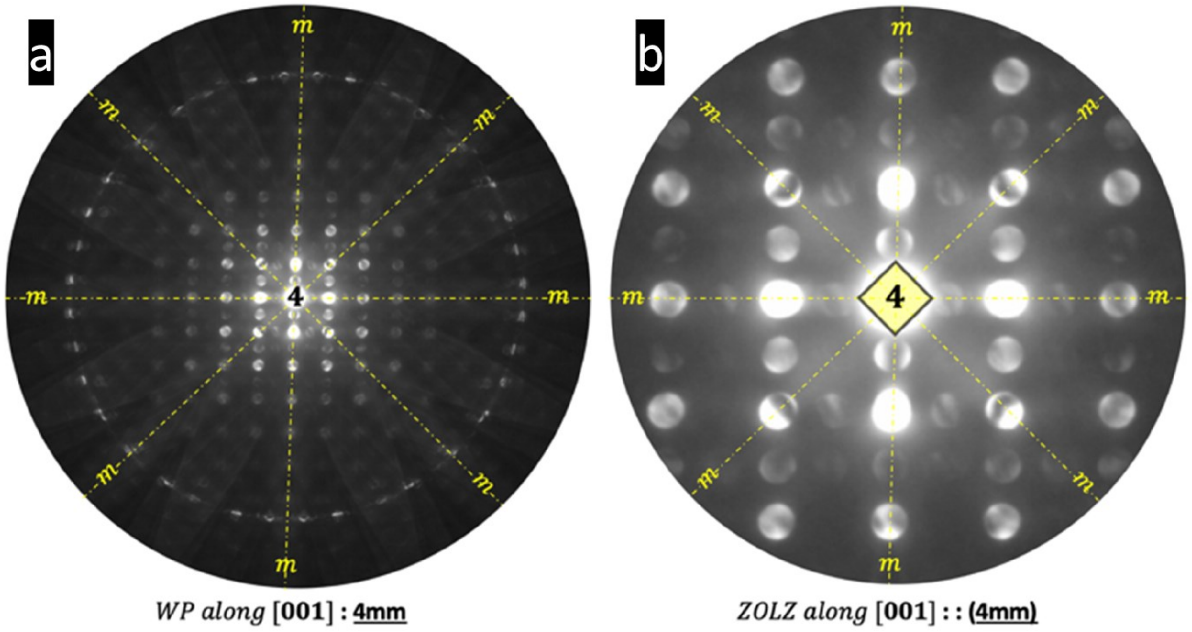

Figure 4

Convergent beam electron diffraction (CBED) pattern recorded along [001] zone axis. a) the whole pattern ideal symmetry is 4mm, b) the ZOLZ pattern ideal symmetry is also (4mm).

In order to access the single space group, it is necessary to consider the symmetries of the diffraction patterns (CBED or microdiffraction) along the zone axes <100] and/or <110]. This operation is somewhat delicate because the nanosheets are always flat and it is difficult to orient them edge-on.

Another very elegant method to refine the characterization of the BOC is to consider the symmetry of the nanosheet form. This is what we address in the next paragraph.

3.3 Symmetry analysis and morphology, the equilibrium shape

It is firmly established in materials science, through the principles of group theory, that the morphology of phases presents in any medium, whether it be solid, liquid or gas, is of great importance. Extensive efforts have been made to comprehend both the equilibrium shape and the habit plane adopted by these phases within a specific medium (Cahn *et al*. 1982). It is a well-acknowledged fact that the shape of a crystallographic precipitate developing within a solid matrix is determined by the point group, whose elements are shared between the precipitate and the matrix (Cahn *et al*. 1982; Redjaïmia *et al*. 1993; Van Landeghem *et al*. 2015; Skiba *et al*. 2018; Ozturk *et al*. 2020). On the other hand, the shape of a phase occurring in an isotropic medium is solely imposed by the symmetry element of its point group (Buerger *et al*. 1978; Kabbara *et al*. 2019).

We will apply this group theory, based on the symmetry analysis, to explain the shape developed by the BOC nanosheets.

A trace analysis derived from the electron diffraction pattern recorded along [001] (**Fig. 5a**), superimposed on its corresponding TEM image (**Fig.5b**), reveals that the BOC particles adopt a square shape. The lateral faces parallel to the c-axis – *i.e.*, parallel to [001] –, and bounding the square shape are parallel to the following crystallographic planes: (110)), $(\bar{1}10)$) and their opposites.

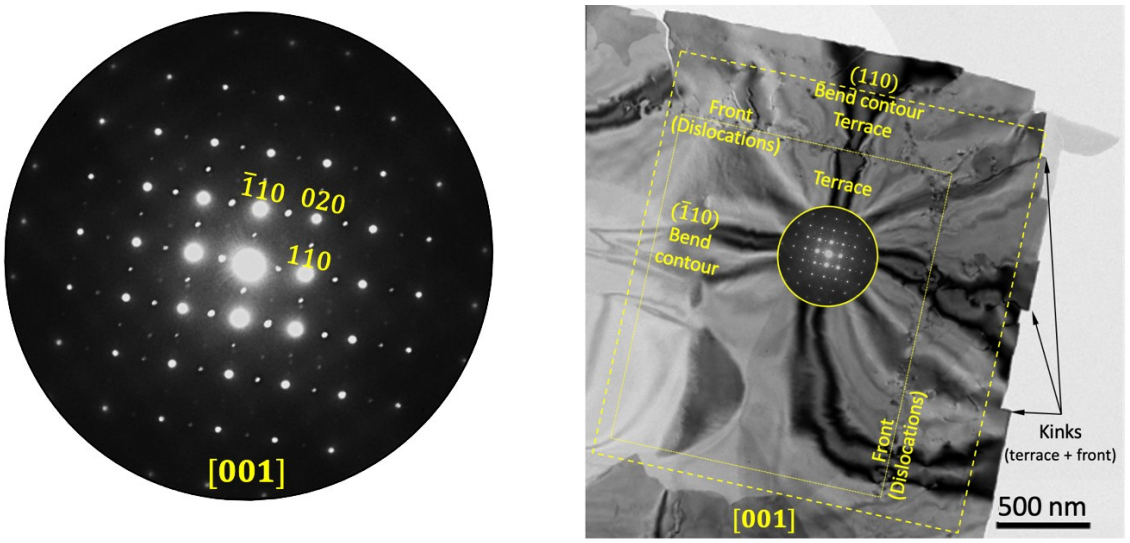

a ***b***

Figure 5

a) Electron diffraction pattern recorded along the [001] zone axis superimposed on the corresponding bright field TEM image of a BOC nanosheet; one can notice the indexed Bend contours. b) Example of bend contours, front dislocations, and kinks present on one nanosheet. The characteristics of these kinks are their (110), $(\bar{1}10)$-oriented terraces and the corresponding front along the $[\bar{1}10]$ and [110] directions, respectively. The corresponding SAED pattern recorded along [001] zone axis is provided in the center.

On the basis of the electron diffraction pattern, we can assert that the BOC particles, belonging to the point group 4mm or 4/m2/m2/m, develop a square shape (through the origin) (Phillips *et al*. 1971). The latter, pedion or pinacoid, are both open forms dictated by the symmetry elements belonging to the

hemihedral point group 4mm or to the holo-symmetric 4/mmm point group, respectively. The pedion is a singled face form parallel to (001) or $(00\bar{1})$ while the pinacoid is a pair of faces parallel to (001). These open forms must also have at least one additional (any) form in order to completely enclose the space surrounding the pedion or the pinacoid.

These two shapes, belonging to 4mm or 4/mmm corresponding both to an absolute extremum (Cahn *et al*. 1982), indicate that the development of the BOC particles is energetically favorable, *i.e.*, a stable BOC nanosheet.

On close inspection of **Fig. 5b**, the convexity of the faces of the BOC nanosheet and the presence of kinks (terrace and front) on lateral faces of the square nanosheet of the BOC particle are apparent.

In **Fig. 5b**, the kinks terraces are parallel to the (110), $(\bar{1}10)$ nanosheet faces and their fronts move parallel to the $[\bar{1}10]$ and [110] directions, respectively.

The HRTEM image recorded along the [100] direction **(Fig. S6)**, presenting the edge of the square nanosheet, points out two perfectly parallel faces. This geometry goes against that of the pedion, a single face orthogonal to the [001] direction, and fits perfectly with that of the pinacoid (pair of parallel planes). Consequently, it is clear that the BOC nanosheet belongs to the point group 4/mmm and not to the 4mm one.

This geometric information indicates that we are in the presence of a pinacoid, *i.e*. a pair of parallel faces (**Table S1**).

The combination of structural and morphological analyses by electron microscopy leads us to, ultimately, affirm that the BOC nanosheet is described by a centred tetragonal Bravais lattice belonging to the point group 4/*mmm* and crystallizing either in the spatial group *I*4/*mmm* (139) or in the spatial group *I*4/*mcm* (140).

The comparison of the theoretical simulations of the diffraction patterns recorded along the [100] zone axis of the space groups $I4/mcm$ and $I4/mmm$ with the FFT of the HRTEM image obtained along the same zone axis [100] (**Fig. 6**), makes it possible to deduce without ambiguity that the space group describing the structure of the BOC is indeed $I4/mmm$ or $I\frac{4}{m}\frac{2}{m}\frac{2}{m}$, in its full notation.

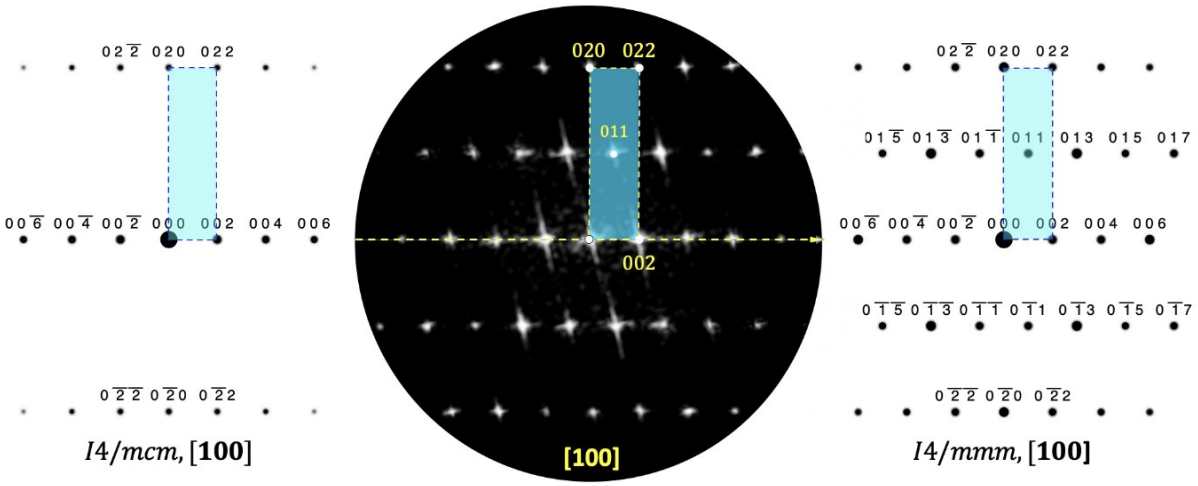

Figure 6
Parallel between the simulations of the diffraction patterns of the space groups I4/mcm and I4/mmm obtained along the zone axis [100] and the FFT of the HREM image of the BOC nanosheet recorded along the same zone axis [100]. We can point out the similarity between the simulation corresponding

to the space group I4/mmm, and the FFT of the experimental HREM of the BOC nanosheet obtained along the same zone axis [100].

To provide additional validation for this deduction, structural characterization was performed by TEM/SAED and further confirmed by XRD measurement (**Figs S7, S8)** in Bragg-Brentano geometry. The XRD data exhibits a flawless alignment with the body centred tetragonal $Bi_2O_2CO_3$ structure, oriented along the [001] direction, further reinforcing this conclusion.

The lattice parameters obtained from SAED patterns recorded along different zone axes ([001] **Figs 4a, 5a** and [100] **Fig. 6b**), are in adequacy with those obtained by X-rays diffraction describing the BOC (**Fig. S8**) and the SAED pattern recorded on a zone with many nanosheets differently oriented (**Fig. S7**), are:

$$a = 3.91 \text{ Å and } c = 13.77 \text{ Å}.$$

We have clearly established, by electron diffraction (SAED, CBED) in combination with symmetry theory, that the crystallographic structure of the BOC is described by the space group I4/mmm ($a = 3.91\ A\ and\ c = 13.77\ A$). This result was confirmed on the atomic scale by TEM images obtained in HAADF-STEM mode (**Fig. S9**) along the zone axes [001], [100] and [110]. The atomic organization along these 3 zone axes thus obtained is in perfect agreement with the simulations carried out with Vesta and CrystalMaker softwares.

To elucidate the arrangement of the nanosheets at the atomic scale, additional to **Fig. S6** investigations were conducted utilizing the HAADF STEM mode, which provides a Z-contrast image. These findings are presented in **Fig. S9**.

To achieve this visualization, cross-sectional views of the nanosheets were attained through the application of the Focused Ion Beam (FIB) technique along two zone axes: [100] and [110]. The resulting images in **Figs. S9b** and **S9c** exhibit high-resolution STEM cross-section views. Additionally, a top view of a nanosheet is presented in **Fig. S9a**.

3.4 Spectroscopy analysis of the nanosheet

To confirm that Bi_2O_3 nanosheets synthesized in water undergo carbonation upon exposure to air, resulting in their conversion into the tetragonal phase of $Bi_2O_2CO_3$, EELS analysis was conducted specifically on the carbon C-K edge, as depicted in **Fig. S10a**.

EELS analysis provides further confirmation, as the fine structure observed in the spectrum at the C-K edge corresponds to the carbonate signal (**Fig. S10a**). Additionally, EFTEM elemental mapping was conducted, revealing a consistent and uniform dispersion of the Bi, O, and C elements within the nanosheets, as illustrated in **Fig. S10b**.

Furthermore, this analysis strongly supports the idea that the synthesized nanosheets have undergone not only oxidation but also carbonation, resulting in the formation of $Bi_2O_2CO_3$. This carbonation process is attributed to exposure to air following the synthesis. The presence of C=O and C-O functional groups indicates additional reactions with carbon dioxide from the ambient environment, ultimately leading to the formation of $Bi_2O_2CO_3$.

The comprehensive data collected from TEM/SAED, XRD, EELS and EFTEM collectively offer compelling evidence supporting the categorization of the EDDL-synthesized nanosheets of $Bi_2O_2CO_3$ within tetragonal centred Bravais lattice and belonging to the $I4/mmm$ (139) space group.

3.5 Growth mechanism of the BOC

The BOC-phase is formed by oxidation and carbonation (reaction with carbon dioxide) of bismuth nanosheets, in contact with water first and air next, after evaporation of the liquid. It is therefore important to understand which mechanism is involved in the formation of bismuth nanosheets in water. In this section, we will try to describe this mechanism which is schematically depicted in **Fig. 7**.

The square shape and the particular dimensions of the particles lead us to question the formation mechanism of these bismuth nanosheet in water, which can be considered as an isotropic medium.

To answer this question, special attention to the diffraction pattern and its corresponding TEM image (**Fig. S6**) is required.

From these figures, further characteristics can be drawn:

- Most of the particle faces are decorated by kinks. The latter are characterized by their terraces and their fronts (**Fig. 5b**).
- The particle lateral faces are convex (**Figs. S4a, S11**) or at least flat (**Figs. 5, S12a-b, S13a**) but never concave

This behavior indicates that the development of the nanosheet proceeds by lateral expansion of the kinks (terrace and front): the front move in the <110] directions parallel to the terrace plane (001). The front can move in opposite direction and sometimes leading to collisions of the fronts and also to the creation of pores having the same geometry as the fronts give rise to them. If the porous zone is continuous (**Fig. S13a**), this leads to a fracture of the nanosheet and the consecutive detachment of the central part of the nanosheet. The later collapses, leaving in the nanosheet a scared area, empty of matter (**Fig. S13b**).

Under specific conditions, which may be linked to production parameters, it is possible for the lateral growth of the four faces to fade or diminish, only to resume under the same crystallographic orientation conditions. This interruption gives rise to a semi-coherent interface. This semi-coherent interface is marked by the presence of dislocations that introduce slight deviations from the initial terrace coherence, ultimately ensuring continuity, as illustrated in **Fig. 5b**.

In some instances, certain BOC nanosheets exhibit jogs, both on the terraces and fronts, which give the impression of a spiral-like development, as depicted in both STEM BF and HAADF modes in **Figs. S11a, b**. In this case, the terraces run parallel to the nanosheet plane, while the corresponding fronts are perpendicular to the nanosheet plane, aligning with the c-axis (// [001]) of the unit cell. This particular geometric arrangement bears resemblance to the development of phase particles along dislocations. It is worth noting that the process of thickening through these jogs, where terraces are parallel to the nanosheet plane while fronts are perpendicular to it, progresses relatively slowly.

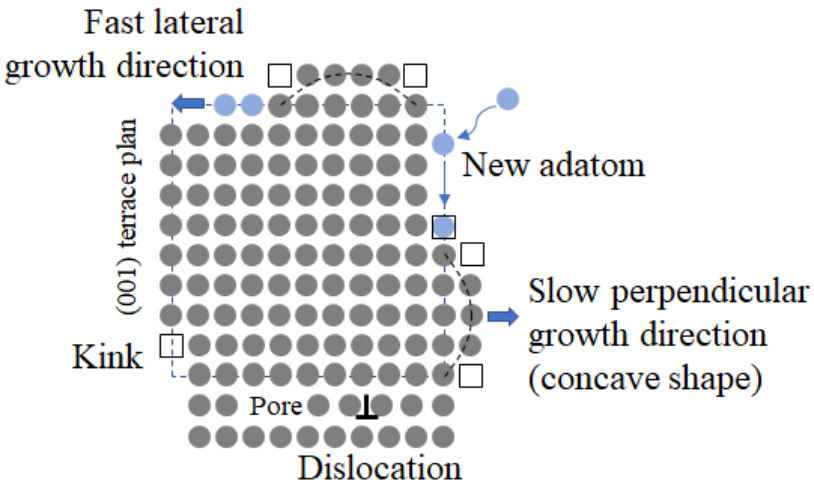

Figure 7
Schematic of the proposed growth mechanism of individual nanosheets.

3.6 Origin of the satellite spots on electron diffraction pattern recorded along [001]

3.6.1 Bend contours

Most nanosheets are crossed by equal inclination fringes or bend contours (**Fig. S14**). These bend contours are change in image contrast indicating that the crystallographic orientation of $(hkl)_i$ planes are equal with respect to the incident beam along $\langle uvw \rangle$ direction. They correspond to exact Bragg diffraction position. When some of these bend contours intersect, they indicate that the corresponding planes $(hkl)_i$ are in relation to zone $\langle uvw \rangle$ *i.e*, $h_i u + h_i v + h_i w = 0$.

The bend contours reflect the fact that the nanosheets are so thin and/or contain crystal defects that they bent elastically leading to rotation of the lattice planes towards diffracting Bragg position. The diffracted beams coming from the intersection domains of the bend-contours lead to $\langle uvw \rangle$ zone axis diffraction patterns. This bend contour phenomenon has been reported by different authors (Viswanath *et al*. 2008; Suito *et al*. 1965; Marczewska *et al*. 2010; Coughlan *et al*. 2018).

The TEM micrograph (**Fig. S14**) recorded along [001] zone axis is decorated by intersecting bend contours. The latter can successively move from one area to another (a, b or c) when the specimen under observation is slightly tilted.

Bright-field Transmission Electron Microscopy (TEM) images of these nanosheets (as depicted in **Figs. 5b, S12, S13a** and **S14**) reveal numerous contrast contours, particularly when the objective aperture is positioned exclusively over the zero beam. Such features are common in materials with thin plate morphologies (Viswanath *et al*. 2008; Suito *et al*. 965). These contours frequently correspond to bend contours (Marczewska *et al*. 2010; Coughlan *et al*. 2018), stemming from the adaptation of thin nanoplates to the uneven surface of the TEM grid. They can also manifest as spider contours. Spider contours can result from strain fields originating from screw dislocations, indicating the presence of these dislocations within the nanoplates (Morin *et al*. 2011).

3.6.2 Satellite, the extra spots

All electron diffraction patterns obtained from the $Bi_2O_2CO_3$ nanosheets exhibit additional satellite reflections, notably along the [001] direction **(Figures 2-5, S13a)** . These satellite reflections are

supplementary spots or diffraction peaks that emerge between the primary diffraction spots. Satellite diffraction lattices are superimposed on the diffraction pattern of the BOC crystallographic structure.

The occurrence of satellite (extra) spots around the reflections of the electron diffraction patterns can occur due to the presence of planar defects such as stacking faults and twins, point defects like oxygene vacancies, line defects such as dislocation arrays, spinodal decomposition, multiple (double) diffraction, order-disorder transformation, *etc*. The extra spots have been reported by different authors (Rodrıguez-Gonzalez *et al*. 2006; Ou *et al*. 2008; Shi *et al*. 2019; Xu *et al*. 2013; Zhou *et al*. 2010)

In this study, the origin of these lattices is essentially attributed to two phenomena: multiple diffraction and local disorder-order transformations of the BOC crystal structure, passing from a body centered tetragonal to a primitive Bravais lattice.

The extra-spots in the experimental diffraction patterns **(Fig. 8**), we are interested in, are recorded from the area labelled a, b and c (**Fig. S14**). Due to the low intensity of the extra spots, surface plots are drawn around the reflections of the diffraction patterns recorded along [001] (**Fig. 8**). One can notice that the aspect of the extra lattice depends on the area where the incident electron beam is focused. Based on this aspect, the extra spots can be grouped in two lattices in relation to their origins.

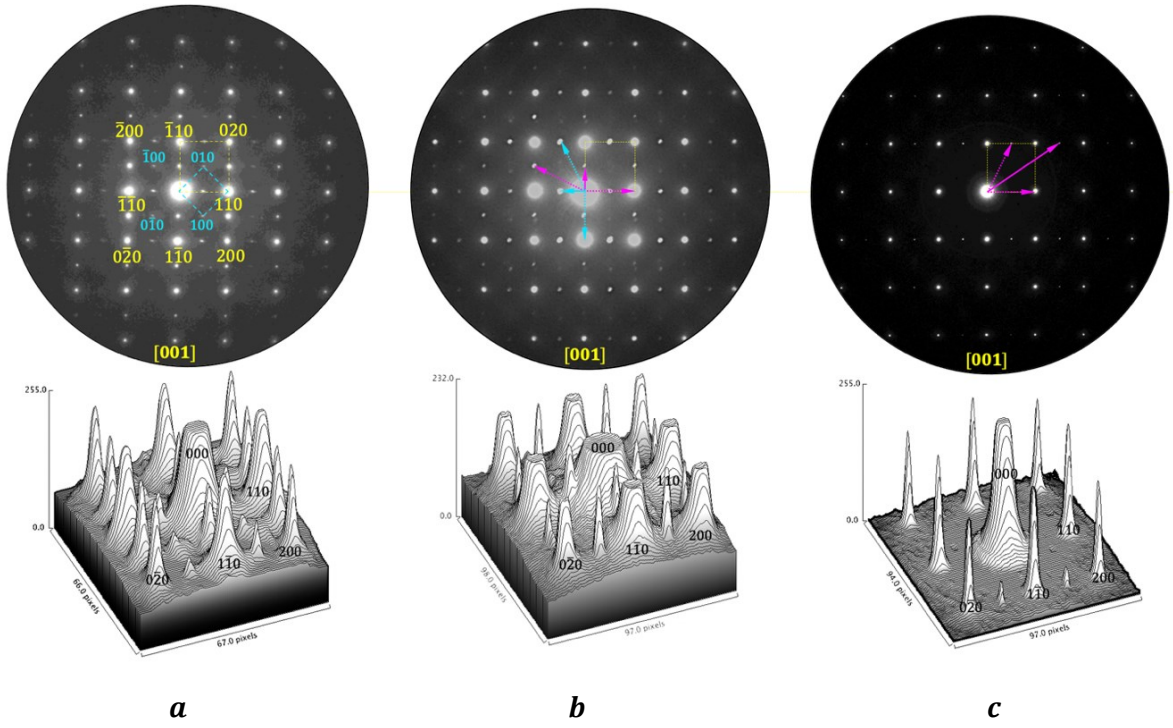

Figure 8
Origin of the extra reflections on the electron diffraction pattern recorded along [001] on different area under the electron beam: **a)** order-disorder transformation (unit cell coloured in cyan), **b)** and **c)** multiple diffraction pointed out by vectors coloured in cyan and/or in magenta.

- The origin of the first one (dashed line colored in cyan, **Fig. 8a**) may come from the disorder-order microstructural transformation of the BOC. The latter loses its centred tetragonal symmetry ($I4/mmm$) and operates a transition towards a structure described by a simple tetragonal ordered cell ($P4/mmm$). The spots are indexed taking into account the simple tetragonal unit cell. One can notice that theses reflections occupy the forbidden position of the centred tetragonal unit cell of the BOC. The lattice parameter of the ordered unit is identical to that of the disordered phase.

- The second group of extra spots is due to multiple diffraction. This phenomenon occurs when two very thin crystals overlap, which have slightly different lattice parameters to each other. The diffracted beam (diffracted wave) by the upper crystal is further diffracted by the lower crystal. In addition to the acquired diffracted patterns belonging to the two crystals, appear extra spots due to the multiple (double) diffraction. The latter could be organized in reflections lattice. It often happens that multiple (double) diffraction spots appear, among others, in diffraction sites (position) prohibited by the structure of the studied crystal(s). This phenomenon is illustrated by the **Fig. 8**. Multiple diffraction paths are indicated by basis vectors colored in cyan (**Fig. 8b**) and/or magenta (**Fig. 8c**).

4. Conclusion

Through this study, we have demonstrated that the synthesis of Bismuthene OxyCarbonate (Bismutite) (BOC) nanosheets (labelled in this study BOC) originates from nano-second pulsed discharges in water, followed by oxydation and carbonation in air. This BOC crystallizes in the body centred tetragonal Bravais lattice (a = 3.91 Å and c = 13.77 Å) nm and belongs to the $4/m2/m2m$ holosymmetric point group and to the $I4/mmm$ space group (or $I4/m2/m2/m$ in its full notation).

Based on the group theory (symmetry analysis), the BOC nanosheets exhibit a pinacoid shape, characterized by a pair of parallel planes parallel to (001). This particular shape is unique to the $4/m2/m2/m$ point group and is inherited from the bismuth nanosheets formed in water. Bismuth crystallizes in the trigonal system, and described using a hexagonal unit cell (with lattice parameters: $a = 3.77$Å et $c = 11.38$Å). It belongs to the point group $\bar{3}\frac{2}{m}$ (scalenohedron) and the space group $R\bar{3}\frac{2}{m}$. Energetically, the BOC shape is described by the symmetry element of the 4/mmm point group, which corresponds to an absolute extremum, resulting in a stable state of the nanosheet.

A mechanism, similar to the ledge mechanism (kinks and jogs) initially proposed to explain the formation of thin plates in metallic matrix, was showed to be relevant in this work. However, unlike the plane coherency in the ledge mechanism, the plane compactness plays an important role in the development of the bismuth nanosheets in water, before their subsequent oxidation in the liquid and carbonation in air.

To the best of our knowledge, this study is the first instance of synthesizing Bismuthene OxyCarbonate by the spark discharge, identifying its crystallographic structure, explaining its morphology, and proposing a mechanism for its growth.

It is interesting to report that the Bismuthene OxyCarbonate $Bi_2O_2CO_3$ has been identified by Grice (Grice *et al*. 2020) as crystallizing in the body centred orthorhombic crystal system and belonging to the $Imm2$ (44) space group with the following lattice parameters $\boldsymbol{a = 3.865(2), b = 3.862(2), c = 13.675(6)}$. This characterization was carried out by X-ray diffraction, a technique known to access the lattice parameters with high precision, superior to that obtained by electron diffraction in SAED mode. However, electron diffraction has a great advantage over X-ray diffraction; it directly allows access (imaging and diffraction) to the symmetry (point and space groups) characterizing the structure. Based on this observation, it is clear that BOC crystallizes in the centered tetragonal structure and belongs to the space group $I4/mmm$. This result is comforted by the theory of groups based on symmetry analysis of the morphology of the BOC nanosheet dictated by the point group $4/mmm$.

In a recent study, nanosecond-pulsed spark discharge between two lead electrodes in liquid nitrogen allowed to synthesize hexagonal lead nanosheets with the following characteristics: $6/mmm$ and $P6/mmm$ as point and space groups, hexagonal prism as morphology, ledge mechanism as process

growth (Kabbara *et al*. 2019). In the same way, the bismuth allowed the synthesis of pinacoid belonging to $4/mmm$ and $I4/mmm$ and the same ledge mechanism. Based on the similarities developed in these two studies, we can, instead of a single metal, use a binary alloy (Pb-Bi) or even a HEA.

Acknowledgements

The authors acknowledge the French PIA (programme d'investissements d'avenir) project Lorraine Université d'Excellence (Ref. ANR-15-IDEX-04-LUE) for financial support.

References

Buerger, M. (1978). *Elementary crystallography: an introduction to the fundamental features of crystals*. Cambridge: Massachussetts Institute of Technology Press.

Buxton, B.F., Eades, J.A., Steeds, J.W., & Rackham, G.M. (1976). *Phil. Trans. R. Soc.*, **A281**, 171–194.

Cahn, J. W., & Kalonji, G. (1982). *Solid-solid phase transformations*. New York, 3. Proceedings of the International Conference on Solid-Solid Phase Transformations, edited by Aaronson, H. I., Laughlin, D., Sekerka, R., & Wayman, C.

Carter, D., Williams, B., Barry, C. (2009). *Transmission Electron Microscopy: A Textbook for Materials Science*. Springer publication.

Chen, L., Huang, R., Yin, S. F., Luo, S. L., & Au, C. T. (2012). *Chem. Engin. J*. **193**, 123–130.

Coughlan, C., Guo, Y., Singh, S., Nakahara, S., & Ryan, K. M. (2018). *Chem. Mater*. **30**, 8679–8689.

CrystalMaker software® (http://crystalmaker.com) (1995-2018). Version 10.3.0 CrystalMaker Software Ltd., Oxford, England.

Dong, F., Ho, W. K., Lee, S. C., Wu, Z., Fu, M., Zou, S., & Huang, Y. (2011). *J. Mater. Chem.* **21**, 12428–12436.

Gupta, T., Rosza, N., Sauer, M., Goetz, A., Winzely, M., Rath, J., Naghdi, S., Lechner, A., Apaydin, D. H., Cherevan, A., Friedbacher, G., Foelske, A., Skoff, S. M., Bayer, B. C., & Eder, D. (2022). *Adv. Sustain. Syst.* **6**, 2100326.

Grice, J.D. (2002). *Can. Mineral*. **40**, 693–698.

Huang, H., Tian, N., Jin, S., Zhang, Y., & Wang, S. (2014). *Solid State Sci*. **30**, 1–5.

Li, J., Wu, Z., Zhang, S., Xu, K., Ma, N., Feng, W., Wu, M., Xu, D., Zhang, S., & Shen, J. (2022). *CrystEngComm*. **24**, 1377–1386.

Kabbara, H., Ghanbaja, J., Redjaïmia, A., & Belmonte, T. (2019). *J. Appl. Cryst*. **52**, 304–311.

Madhusudan, P., Zhang, J., Cheng, B., & Liu, G. (2013). *CrystEngComm*. **15**, 231–240.

Morin, S. A., Forticaux, A., Bierman, M. J., & Jin, S. (2011). *Nano Lett.* **11**, 4449–4455.

Marczewska, B., & Marczewski, K. (2010). *Zeitschrift Phys. Chem*. **224**, 795–799

Ni, Z., Sun, Y., Zhang, Y., & Dong, F. (2016). *Applied Surface Science*, **365**, 314–335.

Nominé, A. V., Noel, C., Gries, T., Nominé, A., Milichko, V. A., & Belmonte, T. (2021). *Molecules*, **26**, 7403.

Oh-Ishi, K., & Ohsuna, T. (2020). *Ultramicroscopy*, **212**, 112955.

Ou, D. R., Mori, T., Ye, F., Zou, J., Auchterlonie, G., & Drennan, J. (2008). *Phys. Rev. B*, **77**, 024108.

Ozturk,U., Cabrera, J-M., Calvo, J., Redjaïmia, A., and Ghanbaja., J. (2020). *Mater. Perf. Charact.* **9**, 57–74.

Phillips, F. C. (1971). *An introduction to crystallography*, 4th ed. Singapore: Longman. John Wiley & Sons, Canada.

Porter, D. A., Easterling, K. E. & Sherif, M. Y. (2009). *Phase Transformations in Metals and Alloys*, 3rd ed. Boca Raton: CRC Press.

Qin, H., Yang, Y., Shi, W., & She, Y. (2021). *RSC advances*, **11**, 13731–13738.

Redjaïmia, A., Ruterana, P., Metauer, G., & Gantois, M. (1993). *Phil. Mag. A*, **67**, 1277–1286.

Rodríguez-González, B., Pastoriza-Santos, I., & Liz-Marzán, L. M. (2006). *J. Phys. Chem. B*, **110**, 11796–11799.

Skiba O., Redjaïmia, A., Dulcy, J., Ghanbaja, J., Marcos, G., Caldeira-Meulnotte, N., & Czerwiec, Th. (2018), *Mater. Charact.* **144**, 671–677.

Suito, E., & Uyeda, N. (1965). Special Issue on Electron Microscopy. *Bulletin of the Institute for Chemical Research*, Kyoto University, **42**, 511–541.

Shi, H. L., Zou, B., Li, Z. A., Luo, M. T., & Wang, W. Z. (2019). *Beilstein J. Nanotechnol*. **10**, 1434–1442.

Tian, N., Hu, C., Wang, J., Zhang, Y., Ma, T., & Huang, H. (2022). *Coord. Chem. Rev.* **463**, 214515.

Thomas, G., & Goringe, M. J. (1979). *Transmission electron microscopy of materials.* New York, Chichester, Brisbane, Toronto: John Wiley and Sons.

Umar, A., Ahmad, R., Kumar, R., Ibrahim, A. A., & Baskoutas, S. (2016). *J. Alloys Comp*. **683**, 433–438.

Van Landeghem, H.P., Gouné M., Bordère, L.S., Danoix, F., and Redjaïmia, A. (2015), *Acta Mater*. **93**, 218–234.

Vesta® software, Momma, K., & Izumi, F. (2011) *VESTA 3 for three-dimensional visualization of crystal, volumetric and morphology data*, *J. Appl. Crystallogr.* **44**, 1272–1276.

Viswanath, B., Kundu, P., Mukherjee, B., & Ravishankar, N. (2008). *Nanotechnol.* **19**, 195603.

Wang, B., Wang, J., Zhang, Y., Mei, Y., & Lian, P. (2017). *Ceram. Int.* **43**, 9310–9316.

Xu, Y. S., & Zhang, W. D. (2013). *Appl. Catal. B: Environ*. **140**, 306–316.

Zhao, T., Zai, J., Xu, M., Zou, Q., Su, Y., Wang, K., & Qian, X. (2011). *CrystEngComm*. **13**, 4010–4017.

Zheng, Y., Duan, F., Chen, M., & Xie, Y. (2010). *J. Molec. Catal. A: Chem.* **317**, 34–40.

Zhou, L., Yu, M., Yang, J., Wang, Y., & Yu, C. (2010). *J. Phys. Chem. C* **114**, 18812–18818.

Supplementary Materials

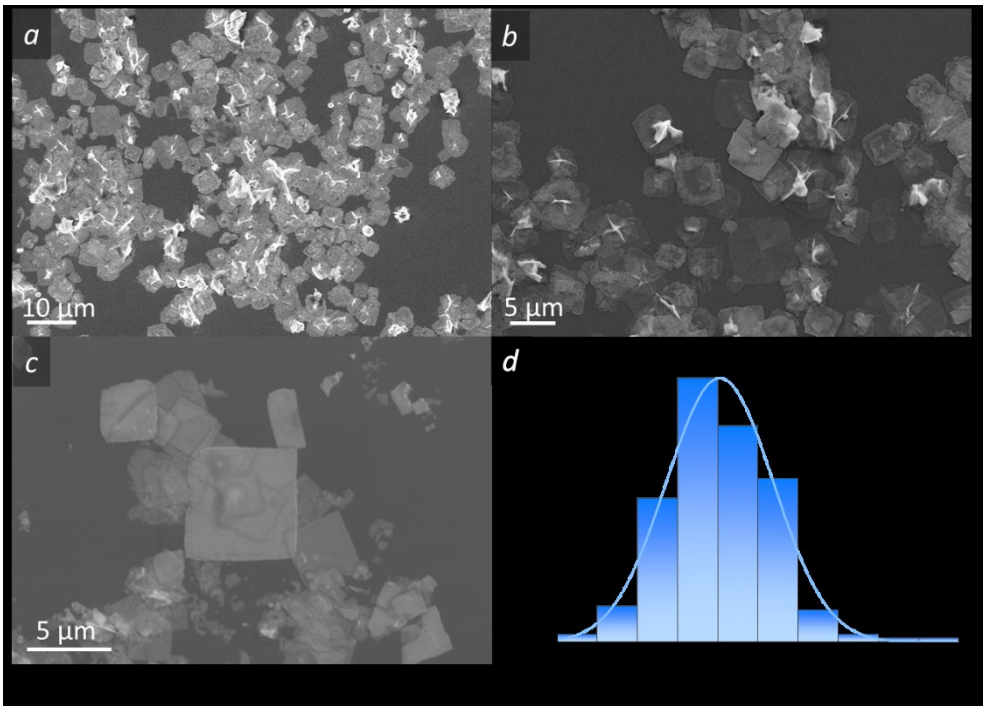

Figure S1

Low-magnification SEM images of a) nanosheets deposited on a Si substrate, b) magnified view of the nanosheets, c) enlarged depiction of a squared sheet, d) lateral size distribution of synthesized nanosheets.

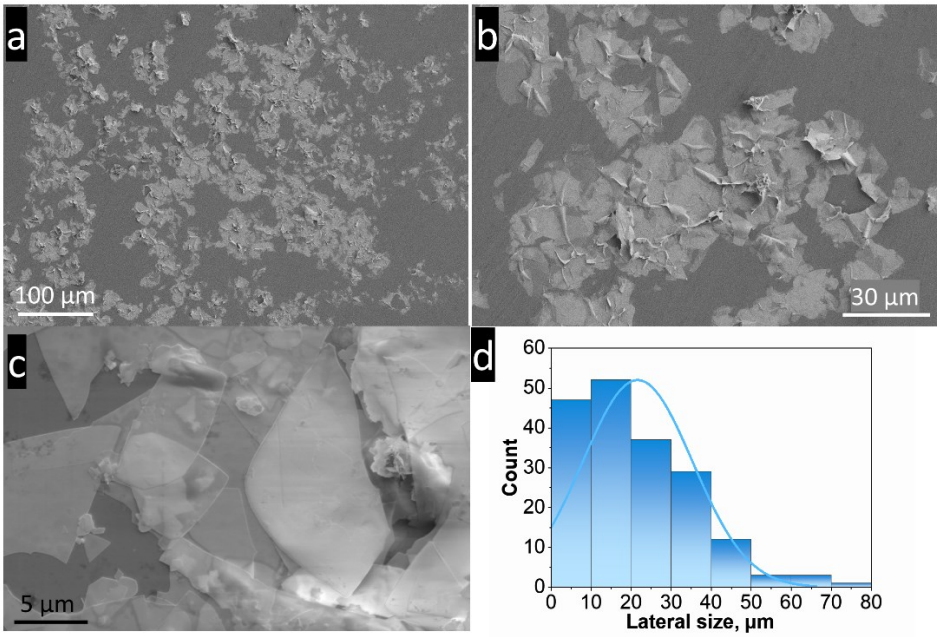

Figure S2

Low-magnification SEM images of a) nanosheets deposited on a Si substrate, b) magnified view of the nanosheets, c) magnified view of a bundle of nanosheets, d) lateral size distribution of synthesized nanosheets

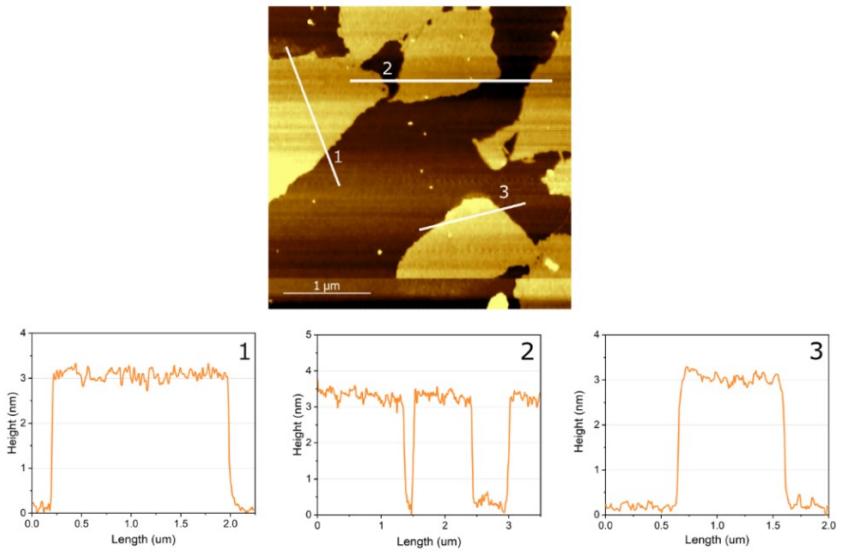

Figure S3

AFM height-sensor micrograph depicting an individual BOC nanosheet. This micrograph provides a one-dimensional step height profile along the white lines labeled as 1-3. Corresponding cross-sections accompany these profiles, offering additional visual information.

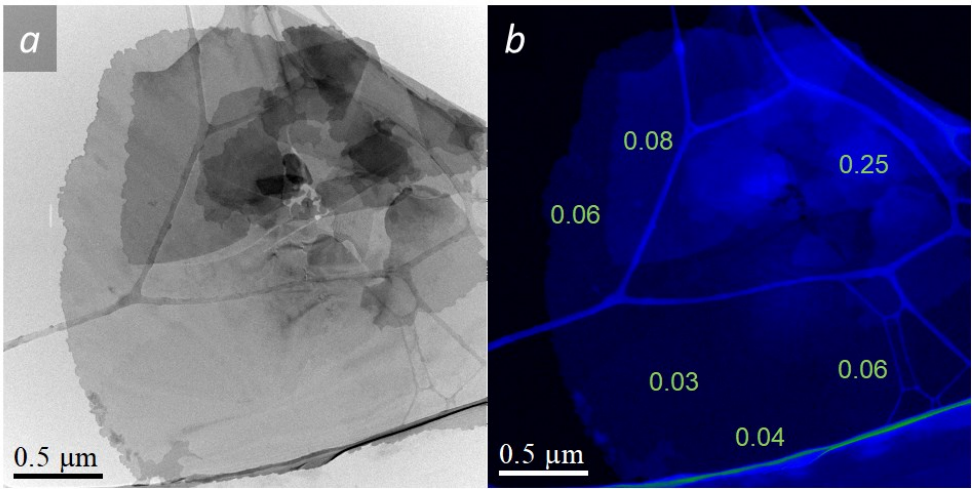

Figure S4

Example of the thin nanosheet a) BF STEM micrograph of a BOC nanosheet deposited on a holey carbon TEM grid with b) corresponding EELS thickness mapping. These mappings indicate the values of the t/λ ratio needed for thickness estimation.

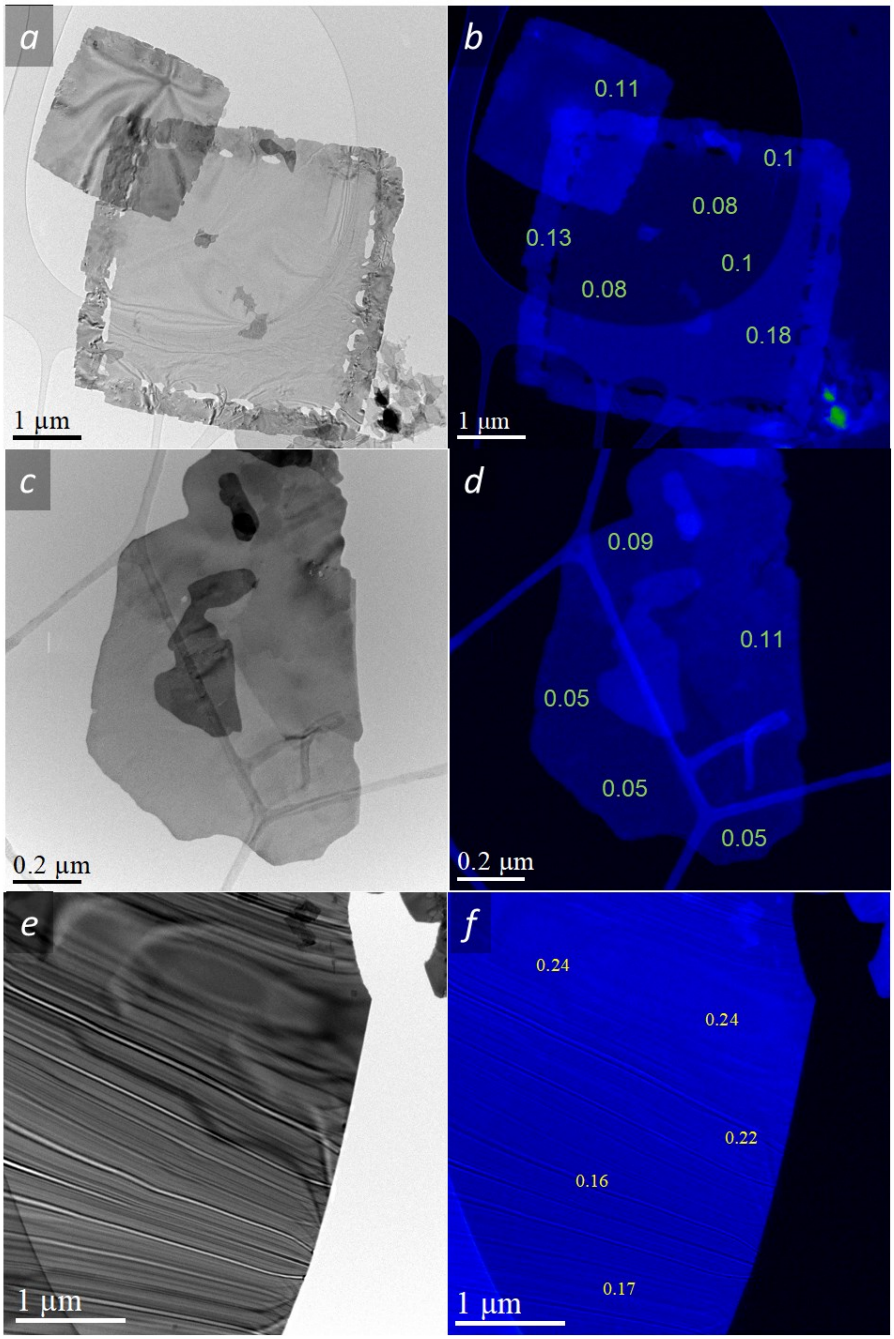

Figure S5

Examples of three nanosheets with different thicknesses : a,c,e) BF STEM micrograph of a BOC nanosheets deposited on a holey carbon TEM grid with b,d,f) corresponding EELS thickness mappings.

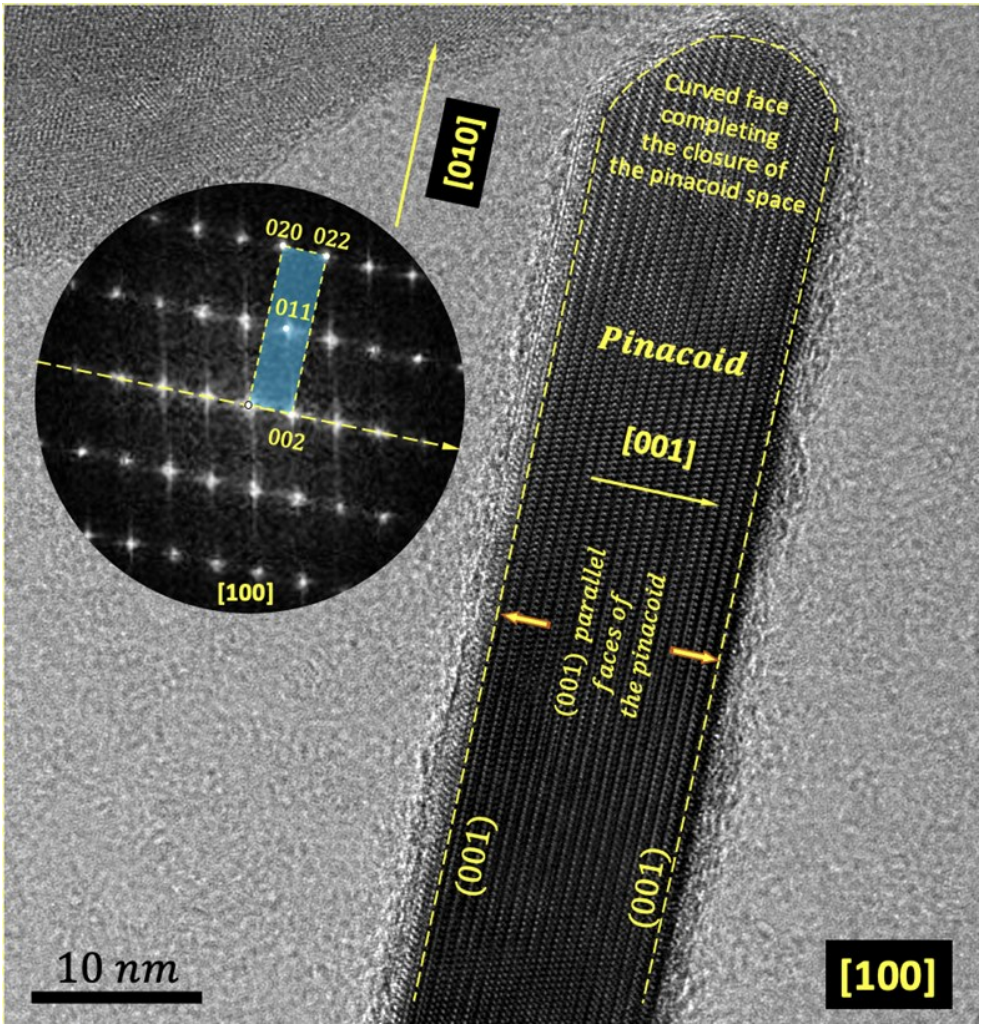

Figure S6

HRTEM image of the BOC nanosheet observed edge-on along the [100] direction. Corresponding FFT along [100] zone axis with the centred tetragonal unit cell. One can notice that the edge-on faces of the nanosheet are parallel to (001) plane as pointed out by the corresponding FFT.

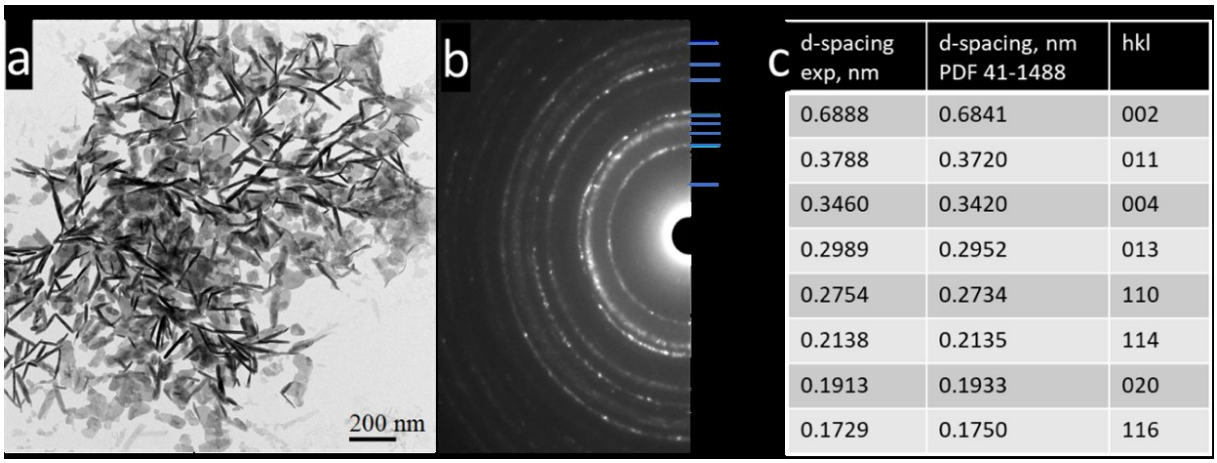

d-spacing exp, nm	d-spacing, nm PDF 41-1488	hkl
0.6888	0.6841	002
0.3788	0.3720	011
0.3460	0.3420	004
0.2989	0.2952	013
0.2754	0.2734	110
0.2138	0.2135	114
0.1913	0.1933	020
0.1729	0.1750	116

Figure S7

a) TEM micrograph of nanosheets with b) corresponding SAED pattern and c) d-spacings indexed to $Bi_2O_2CO_3$ (JCPDS card 41-1488)

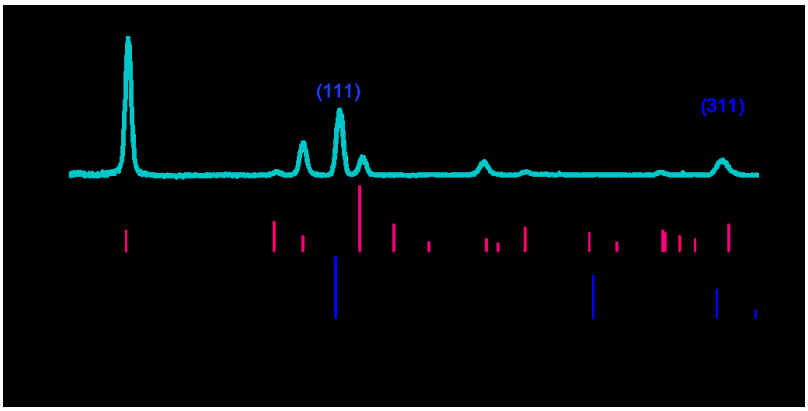

Figure S8

XRD pattern of the nanosheet measured in Bragg-Brentano geometry. Comparison is made between the experimental pattern obtained with λ_{Co} = 1.78897 Å and the reference data from JCPDS 41-1488, corresponding to $Bi_2O_2CO_3$ with the space group I4/mmm.

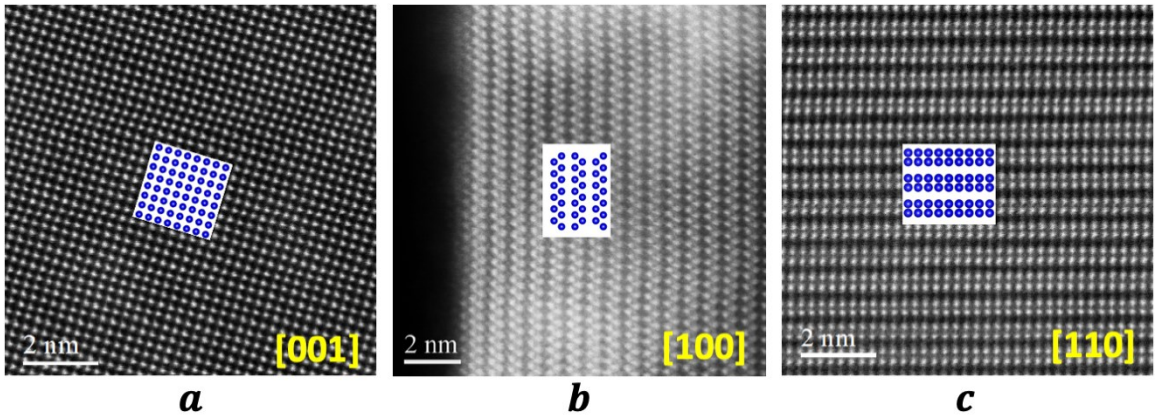

Figure S9

High Resolution images of the BOC nanosheet and simulation **a)** HAADF micrograph recorded along [001] zone axis **b) and c)** STEM FIB cross section micrographs recorded along [100] and [110], respectively. Inserted the corresponding simulated images of the BOC nanosheet using the Vesta Software. Only the Bismuth atoms (High Z) are highlighted in the three simulations.

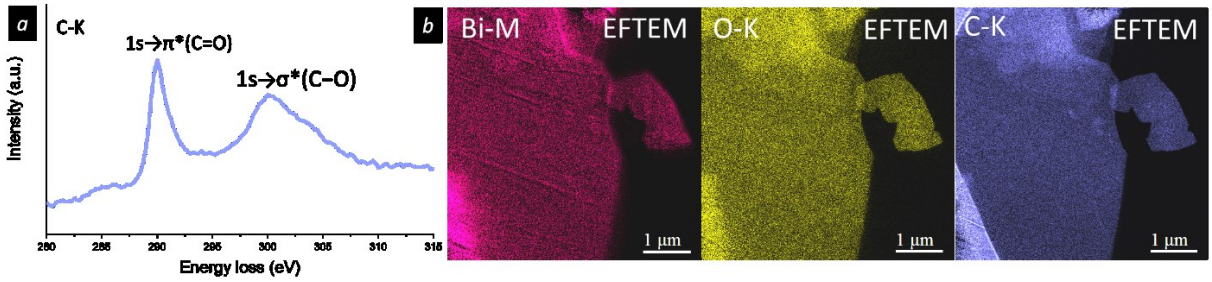

Figure S10

a) EELS spectrum showing the presence of carbonate functional groups, b) EFTEM elemental mapping of $Bi_2O_2CO_3$ nanosheets deposited on a holey carbon TEM grid.

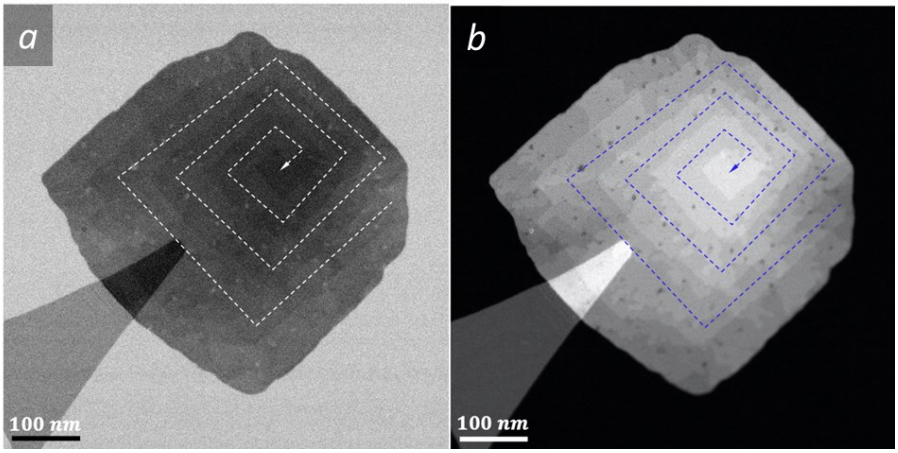

Figure S11

a) TEM-Bright Field micrography showing the BOC nanosheet developed by jog (terrace // (001) and front // [001]) effect reminiscent of a spiral development. b) Corresponding TEM-Dark field. The dashed lines point out the spiral effect.

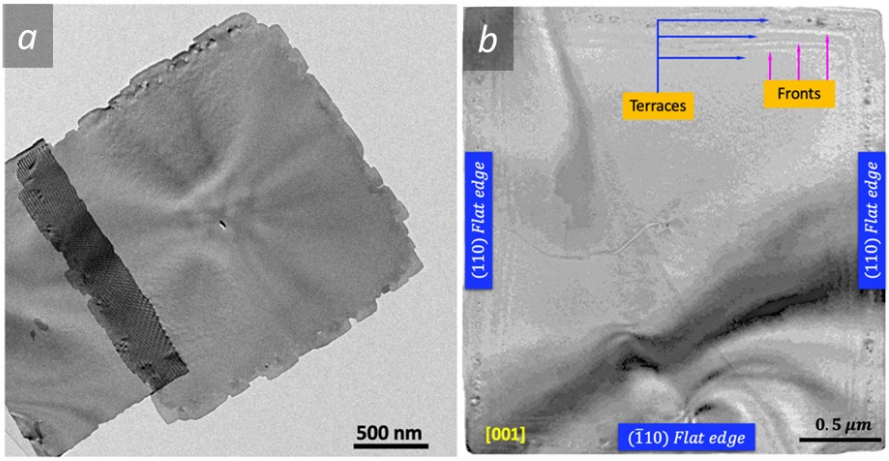

Figure S12

Bright Field TEM images showing squared shape of BOC nanosheets with a) serrated edges by kinks (terraces and fronts) and b) flat edges (with no apparent kinks). One can notice the presence of terraces and fronts on the projected surface.

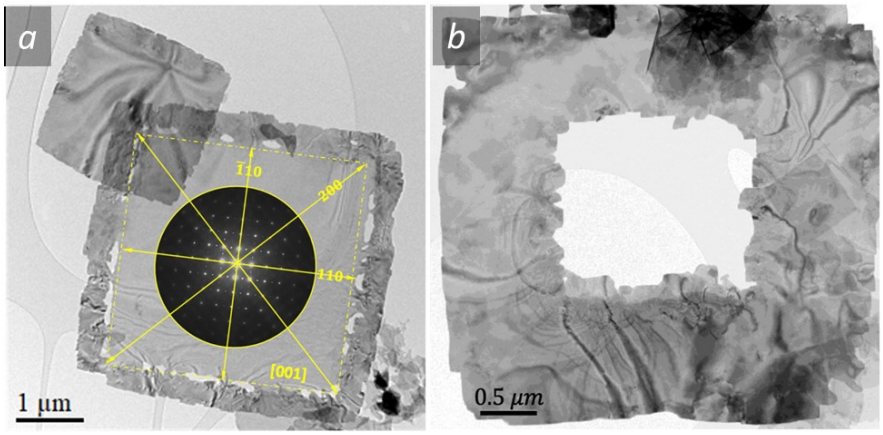

Figure S13

a) Collision between kinks, whose terraces are offset from each other and fronts are of different heights, leading to a porous zone. b) If the porous zone is continuous, this leads to a fracture of the nanosheet; the centre of the nanosheet collapses, leaving in the nanosheet a scared area, empty of matter.

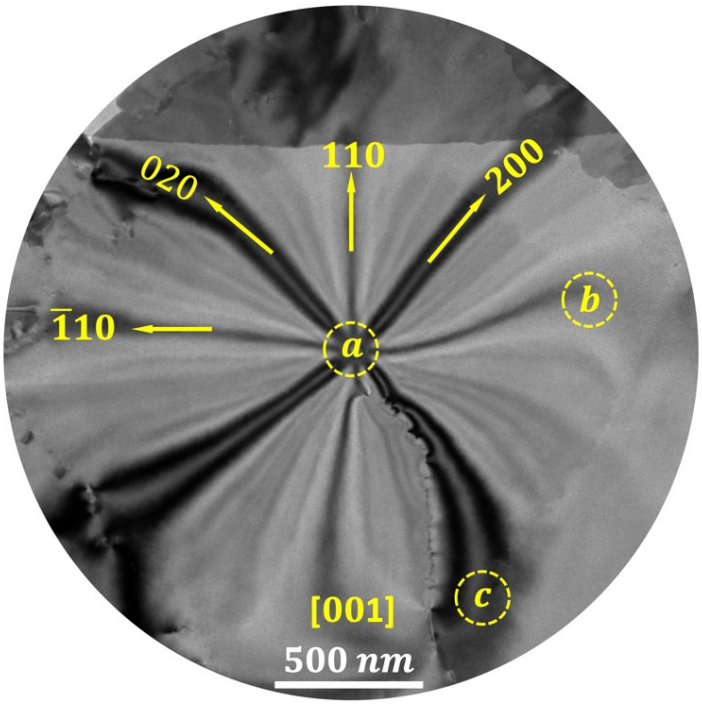

Figure S14

BF TEM micrograph recorded along [001] zone axis decorated by intersecting bend contours. The intersection of the bend contours can move from one area to another (a, b or c) when the specimen under observation is slightly tilted.

Table S1

Crystal forms for the Tetragonal System dictated by the corresponding point Groups.

Crystal system ⟹		*Tetragonal*						
Crystal forms (11)	# Faces	Point groups						
		4	**$\bar{4}$**	**$4/m$**	**422**	**$4mm$**	**$\bar{4}2m$**	**$4/mmmm$**
1. Pedion	1	$001, 00\bar{1}$				$001, 00\bar{1}$		
2. Pinacoid	2		001	001	001		001	001
3. Tetragonal prism	4	$hk0$	$hk0$	$hk0$	$100, 110$	$100, 110$	$100, 110$	$100, 110$
4. Ditetragonal Prism	8				$hk0$	$hk0$	$hk0$	$hk0$
5. Tetragonal pyramid	4	$\boldsymbol{hkl}$				$h0l, hhl$		
6. Tetragonal disphenoid	4		$\boldsymbol{hkl}$				$hhl, h\bar{h}l$	
7. Tetragonal bipyramid	8			$\boldsymbol{hkl}$	$h0l, hhl$		$h0l$	$h0l, hhl$
8. Tetragonal trapezohedron	8				$\boldsymbol{hkl}$			
9. Ditetragonal pyramid	8					$\boldsymbol{hkl}$		
10. Tetragonal scalonohedron	8						$\boldsymbol{hkl}$	
11. Ditetragonal bipyramid	16							$\boldsymbol{hkl}$
Class ⟹		Tetragonal pyramidal	Tetragonal disphenoidal	Tetragonal dipyramidal	Tetragonal trapezohedral	Ditetragonl pyramidall	Tetragonal scalenohedral	Ditetragonal dipyramidal